

## Article

# Novel Tetragonal Boron Pnictides BX (X = N, P, As, Sb, Bi) with Square B2X2 Motifs from Crystal Chemistry and First Principles

Samir F. Matar<sup>1</sup> and Vladimir L. Solozhenko<sup>2,\*</sup> <sup>1</sup> Lebanese German University (LGU), Jounieh P.O. Box 206, Lebanon<sup>2</sup> LSPM–CNRS, Université Sorbonne Paris Nord, 93430 Villetaneuse, France

\* Correspondence: vladimir.solozhenko@univ-paris13.fr

**Abstract:** Novel tetragonal ( $P4_2/mmm$ ) boron pnictides BX (X = N, P, As, Sb, Bi) with chromium boride (**crb**) topology exhibiting a square B2X2 motif with resulting edge- and corner-sharing tetrahedra were predicted from crystal chemistry and extensively characterized by density functional theory (DFT) calculations. All new BX phases were found to be cohesive with decreasing cohesive energy along the series. Mechanically stable with positive sets of elastic constants, all **crb** phases exhibit slightly lower hardness than other BX polymorphs due to increased openness of the crystal structures. All-positive phonon frequencies characterize the **crb** BX family except for X = Bi, which shows a slight acoustic instability; also, the shape of the phonon spectra changes from band-like for X = N, P, As to flat bands for the heavier elements. The electronic band structures reveal insulating to semiconducting properties for **crb** BX, depending on the pnictogen nature along the series.

**Keywords:** boron pnictides; DFT; crystal structure; elastic constants; hardness; phonons; electronic band structures



**Citation:** Matar, S.F.; Solozhenko, V.L. Novel Tetragonal Boron Pnictides BX (X = N, P, As, Sb, Bi) with Square B2X2 Motifs from Crystal Chemistry and First Principles. *Crystals* **2024**, *14*, 359. <https://doi.org/10.3390/cryst14040359>

Academic Editor: Antonio Frontera

Received: 28 March 2024

Revised: 5 April 2024

Accepted: 9 April 2024

Published: 11 April 2024



**Copyright:** © 2024 by the authors. Licensee MDPI, Basel, Switzerland. This article is an open access article distributed under the terms and conditions of the Creative Commons Attribution (CC BY) license (<https://creativecommons.org/licenses/by/4.0/>).

## 1. Introduction

The prediction of novel phases with advanced properties (chemical, thermal, mechanical, electronic, etc.) is a crucial research topic, for which theoretical approaches have recently been developed including computational materials discovery using evolutionary crystal structure prediction [1] and deep machine learning [2]. Despite the availability of structure discovery tools such as Universal Structure Predictor: Evolutionary Xtallography (USPEX) [3] and machine learning programs such as Graph Networks for Materials Exploration (GNoME) [2], the rationalizing role of the scientist (crystallographers, physicists, and chemists) remains unavoidable to establish the relationship between structure, crystal chemistry, and properties to find the optimal way to synthesize new materials. Validation of new structures and stoichiometries requires the support of first principles quantum mechanics calculations within the framework of density functional theory (DFT) [4,5]. A protocol for these calculations is described in the following section. In terms of symmetry, new predicted phases can be analyzed for topology using the online program TopCryst [6].

In 2013, Prasad et al. [7] reported a new hypothetical carbon allotrope called “suaroglitter” with C<sub>8</sub> stoichiometry. The designation as “-glitter” is due to the presence of sp<sup>2</sup> carbon (in addition to the tetrahedral sp<sup>3</sup> carbon) in the structure, which shows similarity to the previously announced C<sub>6</sub> “glitter” [8]. Both carbon allotropes are electrically conductive due to the presence of sp<sup>2</sup> carbon. C<sub>8</sub> “suaroglitter” belongs to the chromium boride (**crb**) topology, which is a large family of carbon allotropes presented in the SACADA database [9]. The **crb** topology archetype is identified as SACADA ID 60; the structure is shown in Figure 1a. The polyhedral representation on the right shows a characteristic central square of sp<sup>3</sup> carbons bonded to form 2 × 2 edge-sharing tetrahedra that are corner-sharing along the *c*-axis. The crystal structure belongs to space group *I4/mmm* (No. 139) (Table 1), with all eight carbon atoms occupying a single Wyckoff position, namely (8*h*).

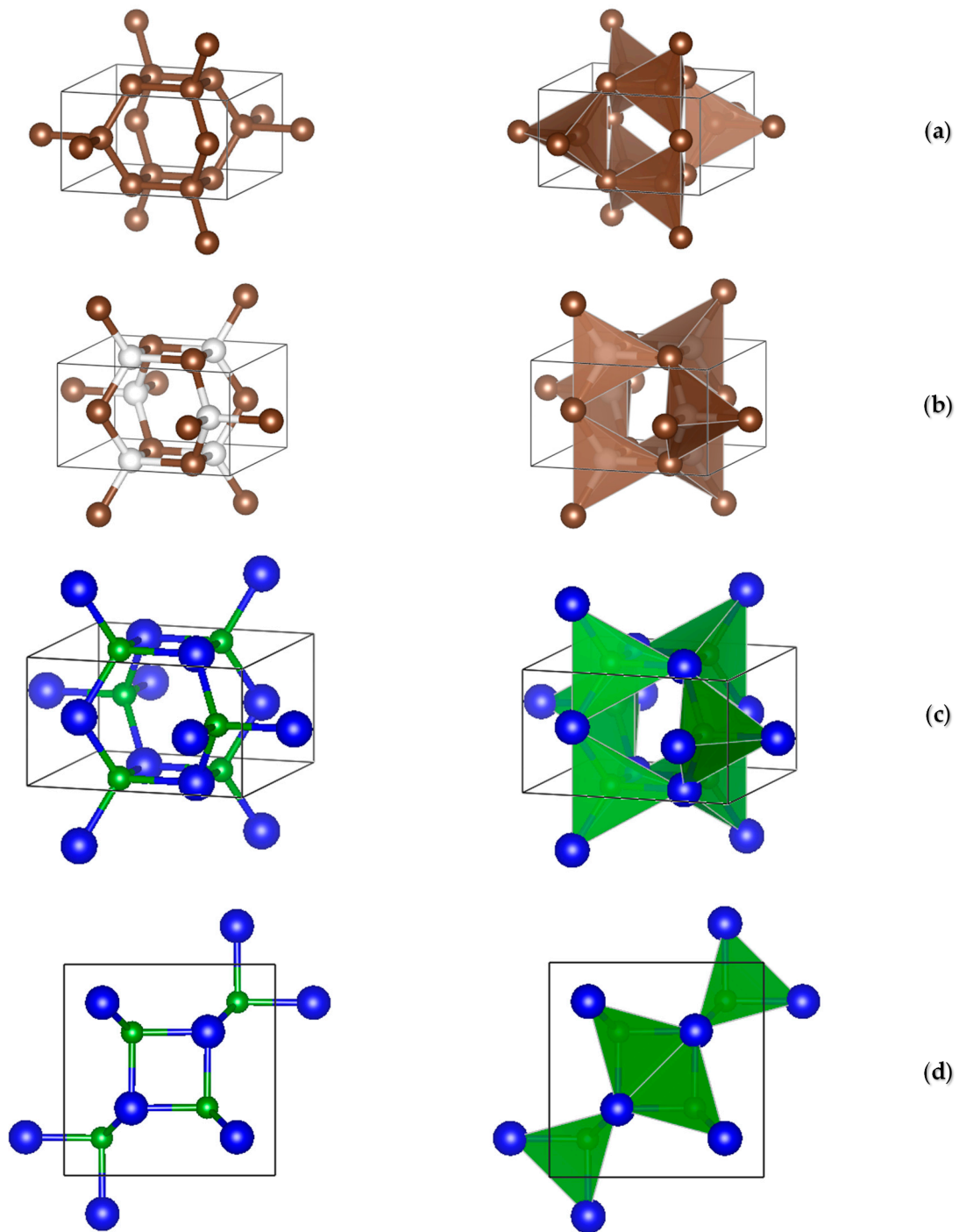


**Figure 1.** Crystal structures (ball-and-stick and tetrahedral representations) of body-centered tetragonal  $C_8$  (a); primitive tetragonal  $(C1)_4(C2)_4$  in which two carbon substructures  $C1$  ( $4g$ ) (white spheres) and  $C2$  ( $4g$ ) (brown spheres) allow accommodation of two different types of atomic constituents to form tetrahedral boron pnictides with  $crb$  topology (b); novel  $crb$  BX ( $X = N, P, As, Sb, Bi$ ) (green and blue spheres correspond to B and X atoms, respectively) (c); projection of the  $crb$  BX structure onto the  $a-b$  plane showing distorted  $B_2X_2$  square and the edge-sharing tetrahedra connected via corners (d).

**Table 1.** Calculated crystal structure parameters of tetragonal carbon allotropes with **crb** topology.

	<b>crb C<sub>8</sub></b> <i>I4/mmm</i> (No. 139)	<b>crb (C1)<sub>4</sub>(C2)<sub>4</sub></b> <i>P4<sub>2</sub>/mmm</i> (No. 136)
<i>a</i> , Å	4.3665	4.3662
<i>c</i> , Å	2.5045	2.5048
<i>V<sub>cell</sub></i> , Å <sup>3</sup>	47.75	47.75
Density, g/cm <sup>3</sup>	3.34	3.34
Atomic positions	C (8 <i>h</i> ) 0.6803, <i>x</i> , 0.0	C1 (4 <i>g</i> ) 0.3197, − <i>x</i> , 0.0 C2 (4 <i>f</i> ) 0.6803, <i>x</i> , 0.0
Bond lengths, Å	1.519 and 1.574 Å	1.519 and 1.574 Å
Angles (deg.)	∠C-C-C = 90° (within the square) ∠C-C-C = 110.96° (along <i>z</i> direction)	∠C-C-C = 90° (within the square) ∠C-C-C = 110.96° (along <i>z</i> direction)
<i>E<sub>total</sub></i> , eV	−71.33	−71.33
<i>E<sub>total</sub></i> /atom, eV	−2.32	−2.32

In this context of special tetrahedral structural features, we were interested in proposing binary systems with edge- and corner-sharing tetrahedra. For this purpose, the crystal symmetry was redefined in a primitive space group *P4<sub>2</sub>/mmm* (No. 136) with two four-fold Wyckoff positions, which is also identified with the **crb** topology. Figure 1b displays the two alternating carbon sites, represented by brown and white spheres, with the structural parameters provided in Table 2, which shows the same interatomic distances and cell volume (cf. Table 1) during the transformation from C<sub>8</sub> to (C1)<sub>4</sub>(C2)<sub>4</sub>.

**Table 2.** Calculated crystal structure parameters of tetragonal boron pnictides with **crb** topology.

	<b>BN</b>	<b>BP</b>	<b>BA<sub>s</sub></b>	<b>BS<sub>b</sub></b>	<b>BB<sub>i</sub></b>
	<i>P4<sub>2</sub>/mmm</i> (No. 136)				
<i>a</i> , Å	4.398	5.558	5.894	6.453	6.764
<i>c</i> , Å	2.538	3.199	3.392	3.723	3.900
<i>V<sub>cell</sub></i> , Å <sup>3</sup>	49.11	98.88	117.83	155.01	178.43
Shortest bond length, Å	d(B-N) = 1.53	d(B-P) = 1.95	d(B-As) = 2.06	d(B-Sb) = 2.31	d(B-Bi) = 2.38
Angles (deg.)	∠BNB = 85.76 ∠NBN = 112.44	∠BPB = 90.73 ∠PBP = 113.59	∠BA <sub>s</sub> B = 91.23 ∠AsBA <sub>s</sub> = 113.50	∠BS <sub>b</sub> B = 91.36 ∠SbBS <sub>b</sub> = 110.49	∠BB <sub>i</sub> B = 91.79 ∠BiBB <sub>i</sub> = 110.28
Atomic positions	B(4 <i>g</i> ) 0.3258, − <i>x</i> , 0 N(4 <i>i</i> ) 0.6875, <i>x</i> , 0	B(4 <i>g</i> ) 0.3217, − <i>x</i> , 0 P(4 <i>i</i> ) 0.6806, <i>x</i> , 0	B(4 <i>g</i> ) 0.323, − <i>x</i> , 0 As(4 <i>i</i> ) 0.681, <i>x</i> , 0	B(4 <i>g</i> ) 0.3229, − <i>x</i> , 0 Sb(4 <i>i</i> ) 0.6814, <i>x</i> , 0	B(4 <i>g</i> ) 0.3238, − <i>x</i> , 0 Bi(4 <i>i</i> ) 0.6818, <i>x</i> , 0
<i>E<sub>total</sub></i> , eV	−68.86	−50.51	−45.293	−39.45	−35.05
<i>E<sub>coh</sub></i> /FU, eV	−5.12	−2.13	−1.52	−0.60	−0.053
(zinc-blende)	−5.32	−2.39	−1.57	−0.70	−0.60

Atomic energies: *E*(B) = −5.3 eV; *E*(N) = −6.8 eV; *E*(P) = −5.2 eV; *E*(As) = −4.5 eV; *E*(Sb) = −4.0 eV; *E*(Bi) = −3.0 eV.

Very recently, we have ab initio predicted superdense hexagonal boron pnictides BX (X = N, P, As, Sb, Bi) with quartz (**qtz**) topology [10–12]. In the present work, we used the (C1)<sub>4</sub>(C2)<sub>4</sub> template structure to predict and investigate within DFT a new family of tetragonal equiatomic boron pnictides BX with **crb** topology that exhibit only B–X bonds, avoiding energetically unfavorable B–B or X–X bonds. Figure 1d displays the square B2X2 motif that characterizes these structures, along with the resulting edge- and corner-sharing BX<sub>4</sub> tetrahedra.

Note that all hypothetical tetragonal BX phases are isoelectronic with **crb** C<sub>8</sub>, i.e., with a valence electron number of 32 (8 × 4), and are therefore expected to exhibit insulating to semiconducting electronic band structures as shown in the present paper.

The present study examines a family of isostructural and isoelectronic boron pnictides to identify trends in the underlying physics. These investigations report on the **crb** BX ground state energies (cohesive) as well as the energy derived properties, namely, the mechanical and dynamic stabilities and electronic band structures. This assessment aims to understand the ‘structure–crystal chemistry–physical properties’ relationship throughout the series.

## 2. Computational Framework

The quantitative search for the ground state energies, the ground state structures, and the related mechanical and dynamical properties required accurate calculations, which were performed within VASP (Vienna Ab initio Simulation Package (VASP) based on the DFT [13,14]. The atomic potentials with all valence states (especially with respect to such light elements as boron and carbon) were considered using the projector augmented wave (PAW) method [14,15]. DFT exchange–correlation effects were considered within a generalized gradient functional (GGA) according to Perdew, Burke, and Ernzerhof [16]. The relaxation of the atoms to the ground state structures was performed with the conjugate gradient algorithm according to Press et al. [17]. The Blöchl tetrahedron method [18] with corrections according to the Methfessel and Paxton scheme [19] was used for geometry optimization and energy calculations, respectively. Brillouin-zone (BZ) integrals were approximated using a special **k**-point sampling according to Monkhorst and Pack [20]. The structural parameters were optimized until the forces on the atoms were below 0.02 eV/Å, and all stress components were below 0.003 eV/Å<sup>3</sup>. The calculations were converged at an energy cut-off of 400 eV for the plane-wave basis set regarding the **k**-point integration in the reciprocal space from  $k_x(6) \times k_y(6) \times k_z(6)$  up to  $k_x(12) \times k_y(12) \times k_z(12)$  for the final convergence and relaxation to zero strains. In the post-treatment process of the ground state electronic structures, the charge density projections were operated onto the carbon atomic sites. The elastic constants C<sub>ij</sub> and the phonon band structures were calculated to evaluate the mechanical and dynamic stabilities. The electronic band structures were obtained using the all-electrons DFT-based ASW method [21] and the exchange correlation GGA functional [16].

## 3. Crystal Chemistry

### 3.1. Developing Binary Equiatomic Compounds

As mentioned above, the archetypical **crb** C<sub>8</sub> carbon allotrope belongs to body-centered tetragonal (“I” centering: from German Innenzentriert) space group *I4/mmm* (No. 139) with a unique carbon eight-fold Wyckoff position (Table 1). This configuration does not permit the occupation of two chemically distinct elements to form a binary compound. From crystal chemistry engineering, **crb** C<sub>8</sub> was redefined in a lower symmetry primitive “P” space group, specifically, *P4<sub>2</sub>/mmm* (No. 136), with two distinct four-fold carbon positions. These positions are described in Table 1 and shown in two different colors (brown and white) in Figure 1b. In both configurations, the C–C distances are 1.519 Å and 1.574 Å (square). These values are on either side of the sum of the atomic radii of two carbon atoms with  $r(\text{C}) = 0.77 \text{ \AA}$ , which is 1.54 Å, i.e., the C–C distance in diamond, the perfectly covalent crystal structure. The cell volume of 47.75 Å<sup>3</sup> is the same in both “I” C<sub>8</sub> and “P” (C1)<sub>4</sub>(C2)<sub>4</sub>, resulting in a density  $\rho = 3.34 \text{ g/cm}^3$  lower than that of diamond:  $\rho = 3.50 \text{ g/cm}^3$  suggesting a slightly lower hardness of both **crb** allotropes. The peculiarity of the structures with **crb** topology is the presence of a C4 square with a perfect angle of 90° and another angle of  $\angle\text{C–C–C1} = 113.62^\circ$ . The building block tetrahedra are distorted, thus showing a clear difference with respect to diamond, where a unique ideal tetrahedral angle of 109.47° is identified.

Using the  $(C1)_4(C2)_4$  template (Table 1), the **crb** binary compounds BX were designed and structurally optimized to the ground state energy following successive calculations with increasing precision of the **k**-space mesh. The results presented in Table 2 show trends of increasing volume with X, which can be explained by the increase in the atomic radius along the 5A column:  $r(N) = 0.75 \text{ \AA}$ ,  $r(P) = 1.10 \text{ \AA}$ ,  $r(As) = 1.20 \text{ \AA}$ ,  $r(Sb) = 1.40 \text{ \AA}$ , and  $r(Bi) = 1.50 \text{ \AA}$ . Note that  $r(B) = 0.83 \text{ \AA}$ . The angles differ from those observed for  $C_8$ , especially for the  $90^\circ$  perfect square angle found below this value in the  $B2X2$  square.

The other relevant result is in the values of the cohesive energies ( $E_{coh}$ ) obtained per formula unit (FU) along the series by subtracting the atomic energies (see footnote, Table 2) from the total energy. The most cohesive structure is **crb**  $C_8$  with  $E_{coh} = -2.29 \text{ eV/atom}$  compared to  $E_{coh} = -2.47 \text{ eV/atom}$  for diamond.

In the BX family, the last row of Table 2 shows the trend of a strong decrease in the cohesive energy counted per FU with a very low magnitude for  $X = Bi$ . Note that for BBi, the electronegativity trend is reversed compared to other boron pnictides,  $\chi(Bi) < \chi(B)$ , so that it can rather be called a “boride”, i.e., with negatively charged boron (see next section for an illustration). At the same time, the cohesive energy of the ambient pressure zinc-blende BX series was added to establish trends. Again, the decrease in cohesive energy along the BX family is confirmed, but to a systematically greater extent than for **crb** BX.

### 3.2. Projection of the Charge Density

Considering the tetragonal **crb** structures of boron pnictides, it is important to establish the relationship between crystal chemistry and crystal structure due to the expected change in ionocovalent character from template  $(C1)_4(C2)_4$  to the BX family, which is caused by the difference in Pauling electronegativities  $\chi$  of pnictogen versus boron. Specifically,  $\chi(C) = 2.55$ , while for the BX family  $\chi(B) = 2.04$ , and for pnictogens  $\chi(N) = 3.04$ ,  $\chi(P) = 2.19$ ,  $\chi(As) = 2.18$ ,  $\chi(Sb) = 2.05$ , and  $\chi(Bi) = 2.02$ , i.e., there is a noticeable decrease in Pauling electronegativity values along the series. The most appropriate qualitative assessment is provided by the description of the charge density projections onto the different **crb** BX phases, which are represented by yellow volumes around the atoms shown in Figure 2.

The **crb**  $C_8$  (Figure 2a), made of a single chemical element, shows a purely covalent character with a tetrahedral charge density around the atoms. This is very similar to diamond, with the difference that, unlike **crb**  $C_8$ , the environment is perfectly tetrahedral, i.e., not distorted. In **crb** BN (Figure 2b) with electronegativity difference of the constituents  $\Delta\chi(B-N) = -1$ , a concentration of charge density around N (grey spheres) is observed, so it can be considered as “boron nitride”. For **crb** BX ( $X = P, As$ ), (Figure 2c,d) with a small electronegativity difference  $\Delta\chi(B-X) \approx -0.15$ , the situation changes with respect to the nitride, and the charge density is almost halfway between B and X. Finally, in BX ( $X = Sb, Bi$ ) (Figure 2e,f), the boron electronegativity is close to that of Sb and higher than that of Bi. Both compounds are rather borides, i.e., with negatively charged boron, as can be observed with the yellow volumes around boron (green spheres).

While the chemical situation of the purely covalent template **crb**  $(C1)_4(C2)_4$  is clear, the BX family exhibits different types of chemical bonding, changing from nitride to an ionocovalent behavior for P and As, and finally to borides in the case of Sb and Bi. It is also important to note that the steric factor plays an important role in these changes, as there is a regular increase in the atomic radius of pnictogen along the series.

After analyzing the crystal chemistry, further investigation is required to fully understand the physical properties, as discussed below.

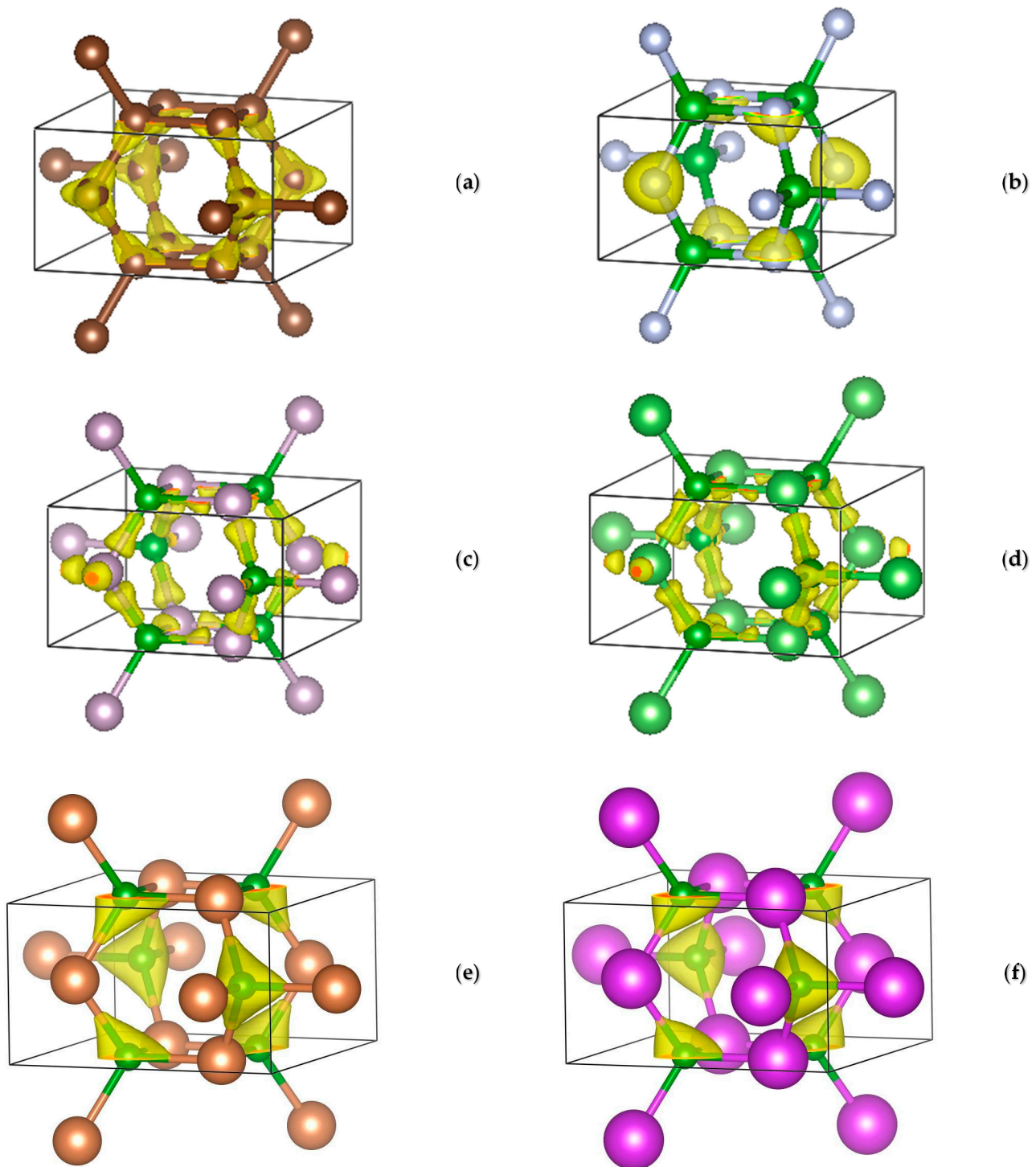


**Figure 2.** Charge density projections (yellow volumes) of body centered tetragonal  $C_8$  (a) and **crb** boron pnictides: BN (b), BP (c), BAs (d), BSb (e), and BBi (f). B atoms are represented by green spheres, while the size of the X spheres is proportional to the respective atomic radius of the pnictogen. The  $c$ -axis is along the vertical direction.

## 4. Results and Discussion

### 4.1. Mechanical Properties from Elastic Constants

The mechanical properties of the novel boron pnictides were studied by calculating the elastic tensors through finite distortions of the lattice. The resulting elastic constants  $C_{ij}$  (where  $i$  and  $j$  correspond to the lattice directions) are presented in Table 3. All  $C_{ij}$

values of all **crb** BX are positive, indicating mechanically stable phases. Along the series, there is a clear tendency for the  $C_{ij}$  values to decrease due to the increase in atomic radii. As expected, the template  $(C1)_4(C2)_4$  has the highest  $C_{ij}$  values, followed by **crb** BN. For heavier pnictogens, a significant decrease in the elastic constants is observed, and for Sb and Bi this decrease is particularly pronounced.

**Table 3.** Elastic constants ( $C_{ij}$ ) of tetragonal boron pnictides with **crb** topology. All values are in GPa.

	$C_{11}$	$C_{12}$	$C_{13}$	$C_{33}$	$C_{44}$	$C_{66}$
$C_8$	949	234	59	1202	323	450
BN	757	174	114	988	239	336
BP	215	165	48	403	83	135
BA <sub>s</sub>	242	71	40	317	77	104
BS <sub>b</sub>	171	60	38	228	58	69
BB <sub>i</sub>	117	48	31	155	40	45

The analysis of the elastic tensors was performed using the ELATE software (<https://progs.coudert.name/elate>) [22], which provides the bulk ( $B$ ), shear ( $G$ ) and Young's ( $E$ ) moduli Poisson's ratio ( $\nu$ ) along different averaging methods; in the present work, the Voigt approach [23] was chosen. Table 4 shows the calculated elastic moduli, with values that follow the trends observed for  $C_{ij}$ .

**Table 4.** Mechanical properties of tetragonal boron pnictides with **crb** topology: Vickers hardness ( $H_V$ ), bulk modulus ( $B$ ), shear modulus ( $G$ ), Young's modulus ( $E$ ), Poisson's ratio ( $\nu$ ), fracture toughness ( $K_{Ic}$ ).

	$H_V$				$B$		$G_V$	$E_V$	$\nu$	$K_{Ic}^*$
	MO <sup>*</sup>	CN <sup>†</sup>	T <sup>‡</sup>	LO <sup>§</sup>	$B_0$ <sup>‡</sup>	$B_V$				
	GPa									MPa·m <sup>1/2</sup>
$C_8$	67	60	93	85	423	423	402	916	0.139	7.1
BN	43	42	53	48	363	367	303	713	0.177	6.0
BP	10	15	28	24	173	151	98	242	0.232	1.4
BA <sub>s</sub>	12	18	22	20	135	123	95	226	0.192	1.3
BS <sub>b</sub>	8	12	17	3	101	94	66	160	0.215	0.8
BB <sub>i</sub>	5	8	13	2	82	68	44	108	0.235	0.5

\* Mazhnik–Oganov model [24]. † Chen–Niu model [25]. ‡ Thermodynamic model [26,27]. § Lyakhov–Oganov model [28].

Vickers hardness ( $H_V$ ) from elastic properties was evaluated using the empirical Mazhnik–Oganov [24] and Chen–Niu [25] models. Hardness was also estimated in the framework of the thermodynamic model [26,27], which is based on thermodynamic properties and crystal structure, and using the Lyakhov–Oganov approach [28], which takes into account the topology of the crystal structure, the strength of covalent bonds, the degree of ionicity, and directionality. Fracture toughness ( $K_{Ic}$ ) was evaluated using the Mazhnik–Oganov model [24]. Table 4 summarizes the Vickers hardness values for all considered **crb** boron pnictides calculated using four models. A tendency of a significant decrease in hardness with increasing atomic number of the pnictogen is observed for all four models. Since it has been shown earlier that the thermodynamic model is the most reliable in the case of boron compounds [12,29,30] and shows perfect agreement with the available experimental data for boron pnictides [31–33], it is obvious that the hardness values calculated within the empirical models are strongly underestimated. The Oganov–Lyakhov model gives slightly

underestimated values for compounds of light pnictogens and does not work in the case of BSb and BBi. It should be noted that all **crb** phases exhibit 4–7% less hardness than other BX polymorphs due to the increased openness of the crystal structures. However, all **crb** boron pnictides are hard phases with Vickers hardness exceeding that of cemented tungsten carbide, the conventional hard material.

The fracture toughness of the new boron pnictides decreases from  $6.0 \text{ MPa}\cdot\text{m}^{1/2}$  for **crb** BN, which is twice that of cubic BN ( $K_{Ic} = 2.8 \text{ MPa}\cdot\text{m}^{1/2}$  [34]), down to  $0.5 \text{ MPa}\cdot\text{m}^{1/2}$  for **crb** BBi.

#### 4.2. Equations of State

The comparative energy trends of different crystalline forms for each boron pnictide can be determined from their equations of state. This was achieved based on a series of calculations of total energy as a function of volume for the zinc-blende (*zb*), rocksalt (*rs*), **qtz**, and **crb** BX polymorphs. The resulting  $E(V)$  curves, shown in Figure 3, were fitted to the third-order Birch equations of state [35]:

$$E(V) = E_0(V_0) + (9/8) \cdot V_0 B_0 [((V_0)/V)]^{2/3} - 1]^2 + (9/16) \cdot B_0 (B_0' - 4) V_0 [((V_0)/V)]^{2/3} - 1]^3,$$

where  $E_0$ ,  $V_0$ ,  $B_0$  and  $B_0'$  are the equilibrium energy, volume, bulk modulus, and its first pressure derivative, respectively. As can be seen from Figure 3, for all boron pnictides, the polymorphs with **crb** topology are metastable over the whole range of experimentally accessible pressures. However, the closeness of the cohesive energies of zinc-blende and **crb** polymorphs (see Table 2) allows for the possibility of the formation of **crb** BX at high pressures and high temperatures as a result of alternative metastable behavior, most likely in chemical reactions of the elements.

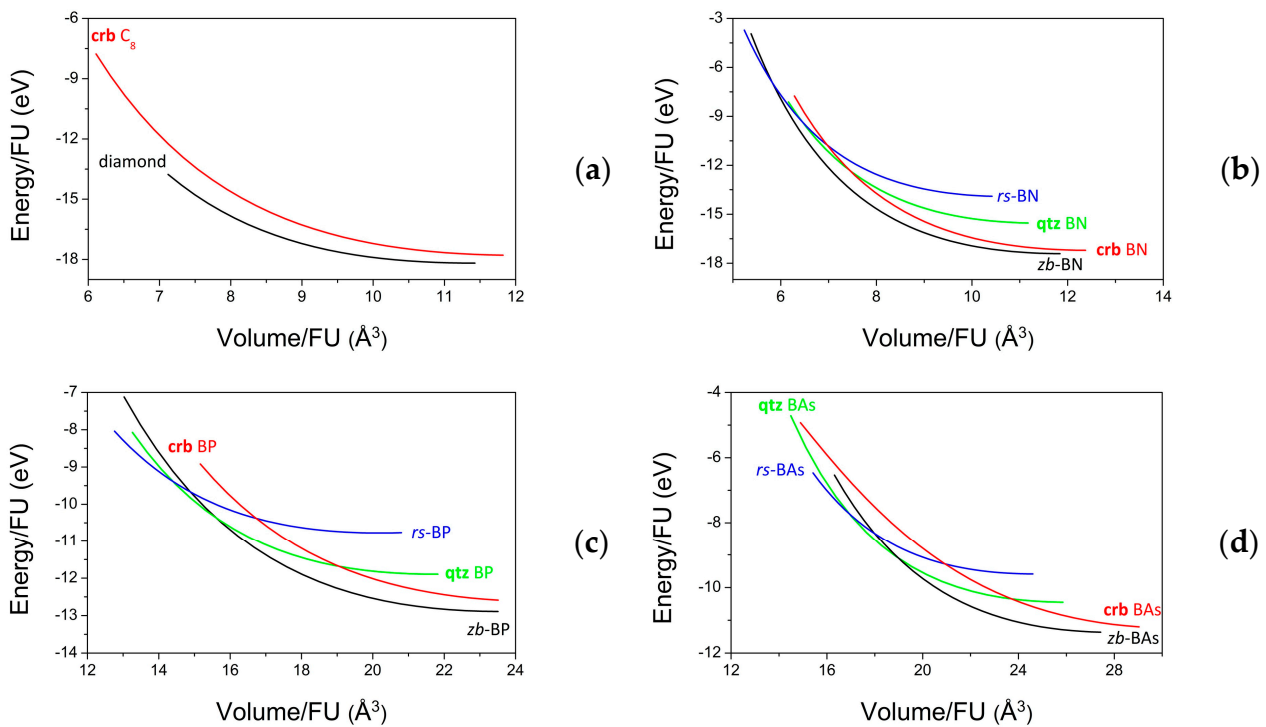
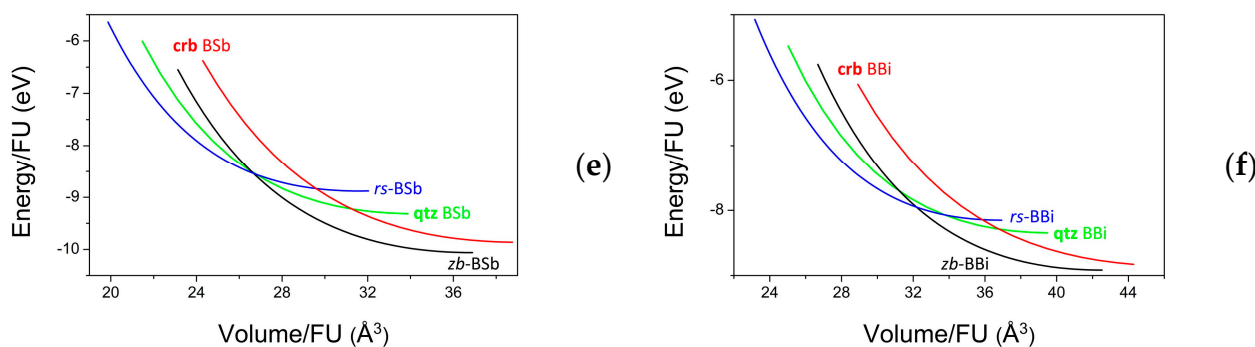


Figure 3. Cont.



**Figure 3.** Calculated total energy per formula unit as a function of volume for carbon allotropes (a) and boron pnictides polymorphs: BN (b), BP (c), BAs (d), BSb (e), and BBi (f).

#### 4.3. Dynamic and Thermodynamic Properties from the Phonons

To verify the dynamic stability of the novel boron pnictides, their phonon properties were studied. The phonon band structures (red lines) obtained from a high resolution of the tetragonal Brillouin zone according to Togo et al. [36] are shown in Figure 4. The horizontal direction corresponds to the main directions of the tetragonal Brillouin zone, while the vertical direction shows the frequencies  $\omega$ , given in terahertz (THz).

The band structures include 3N bands, three acoustic modes starting from zero energy ( $\omega = 0$ ) at the  $\Gamma$  point, the center of the Brillouin zone, up to a few terahertz, and 3N-3 optical modes at higher energies. The acoustic modes correspond to the lattice rigid translation modes of the crystal (two transverse and one longitudinal). All six panels in Figure 4 show positive phonon frequencies, indicating the dynamic stability of all investigated phases. This observation is significant because the **crb** BX phases become less cohesive along the series (Table 2).

The highest frequencies are observed for **crb** C<sub>8</sub> with bands around 40 THz, the signature of the tetrahedral carbon as in diamond [37]. For BX phases, the lower frequencies are observed due to the trend of increasing  $d(\text{B-X})$  along the series (cf. Table 2). This is consistent with the trend of strong decrease in compactness with a change from broad-band behavior for BN (Figure 4b) to progressively flattened bands in BP (Figure 4c), BAs (Figure 4d), BSb (Figure 4d), and finally BBi (Figure 4f), which exhibits a dynamic instability characterized by the negative phonons at the  $\Gamma$  point. These trends are consistent with the decreasing cohesive energy along the series.

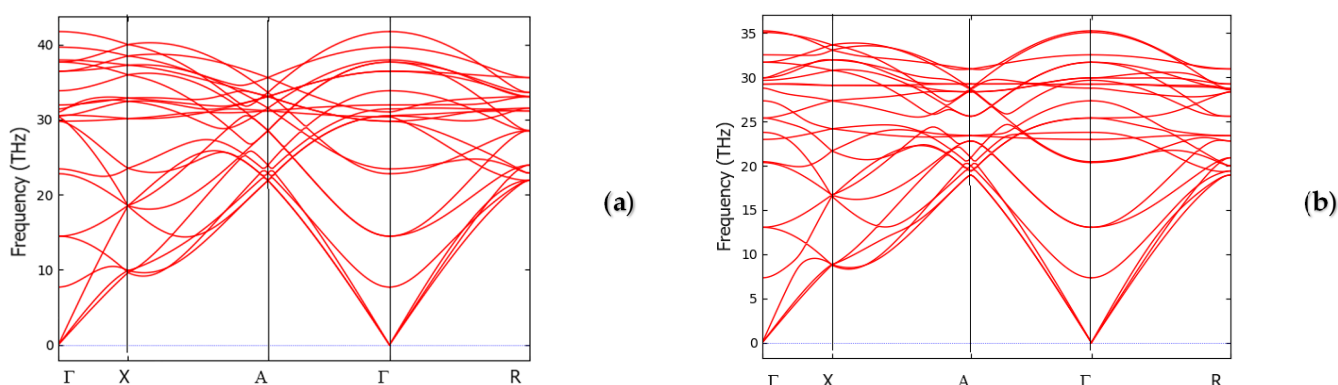


**Figure 4.** Cont.

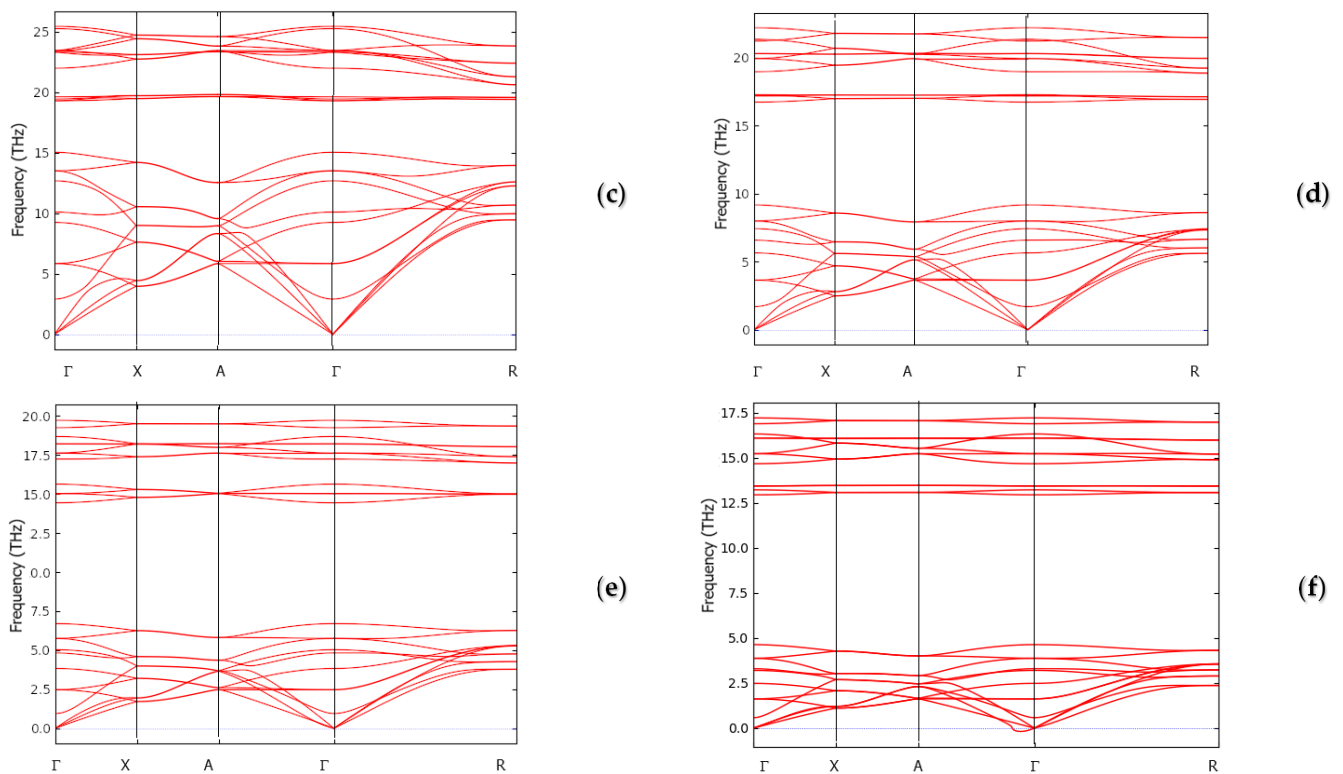


**Figure 4.** Phonon band structures (red lines) of **crb** phases along the major directions of the simple tetragonal Brillouin zone:  $C_8$  (a); BN (b); BP (c); BAs (d); BSb (e); and BBi (f).

The thermodynamic properties of the novel boron pnictides were calculated from the phonon frequencies using the statistical thermodynamic approach [38] on a high-precision sampling mesh in the Brillouin zone. The temperature dependencies of heat capacity at constant volume ( $C_v$ ) and entropy ( $S$ ) of **crb**  $C_8$  and BX are shown in Figure 5 in comparison with available experimental  $C_p$  data for diamond [39,40] and zinc-blende BN [41], BP [42,43], and BAs [44,45]. The observed excellent agreement between the calculated and experimental data for *zb*-BX indicates the validity of the method used to estimate the thermodynamic properties in the case of boron pnictides. For all three boron pnictides, the heat capacity and entropy of **crb** phases are slightly higher than those of *zb*-BX, which is expected for more open **crb** structures compared to the ideal zinc-blende structure.

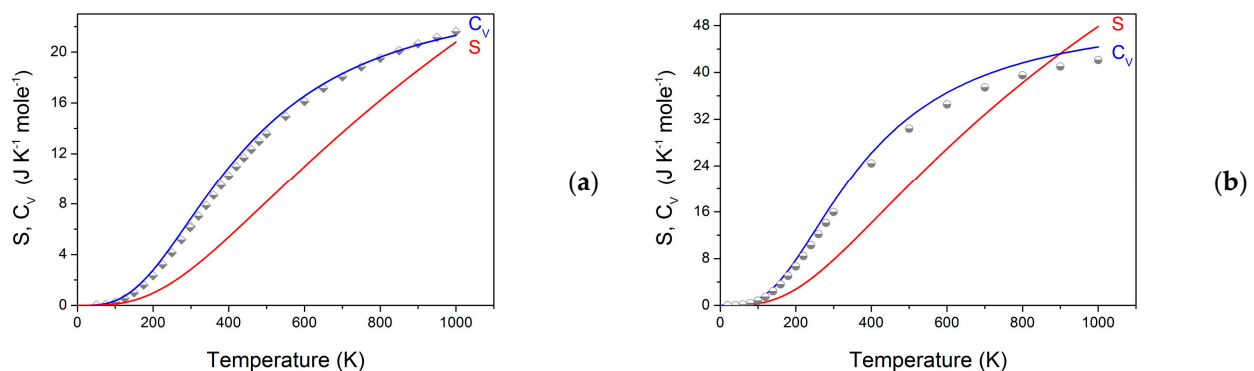


**Figure 5.** Cont.

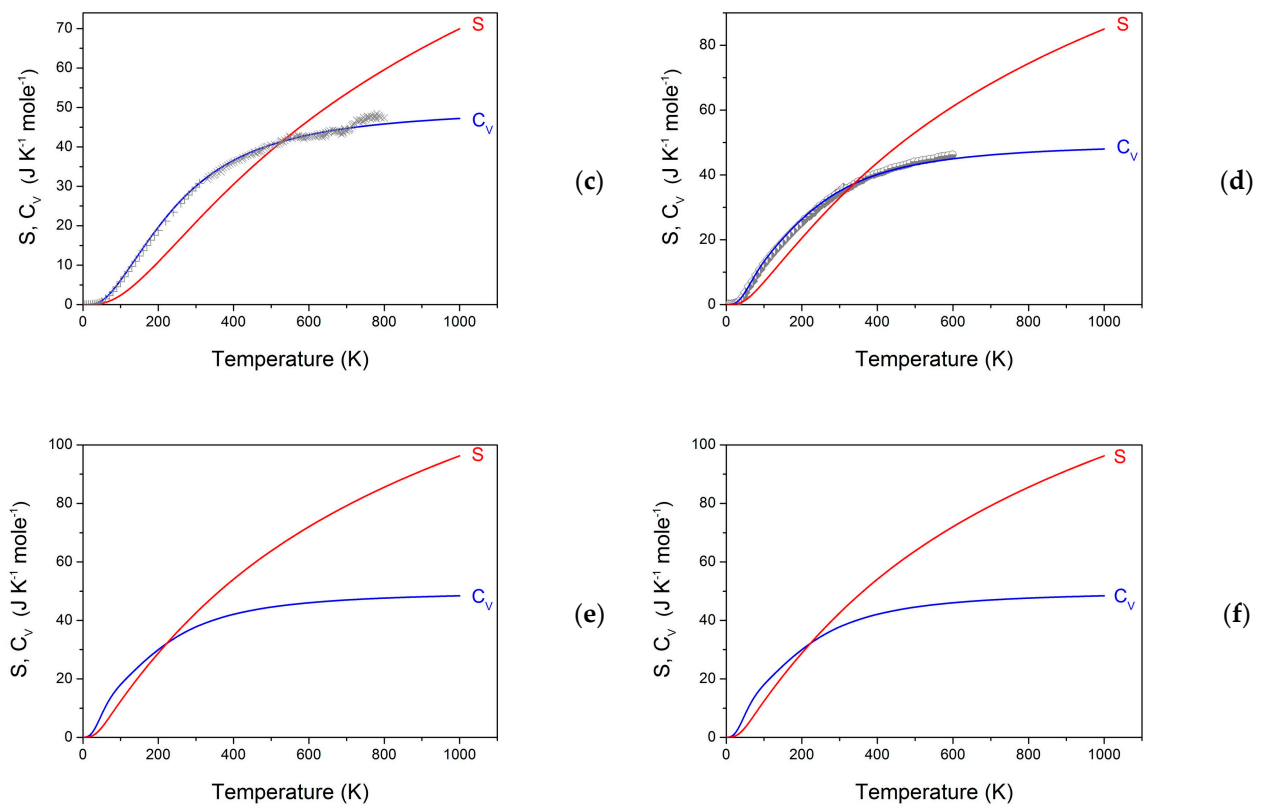


**Figure 5.** Heat capacity at constant volume ( $C_v$ ) and entropy ( $S$ ) of body centered tetragonal  $C_8$  (a) and **crb** boron pnictides as functions of temperature: BN (b), BP (c), BAs (d), BSb (e), and BBi (f). Experimental heat capacity data for diamond and  $zb$ -BX ( $X = \text{N, P, As}$ ) are shown as gray symbols.

#### 4.4. Electronic Band Structures

The electronic band structures of **crb**  $C_8$  and BX were calculated using the all-electrons DFT-based augmented spherical method (ASW) [21]. The results are shown in Figure 6. The bands (blue lines) develop along the main directions of the tetragonal Brillouin zone. The zero energy along the vertical axis is considered with respect to  $E_V$ , the top of the filled valence band VB. All six phases have band gaps ranging from widely insulating in  $C_8$  and BN (the latter presenting the largest band gap  $> 5$  eV), to semiconducting for the other boron pnictides, with the almost closing gap in BBi. This behavior is related to the continuous change in chemical properties described above.

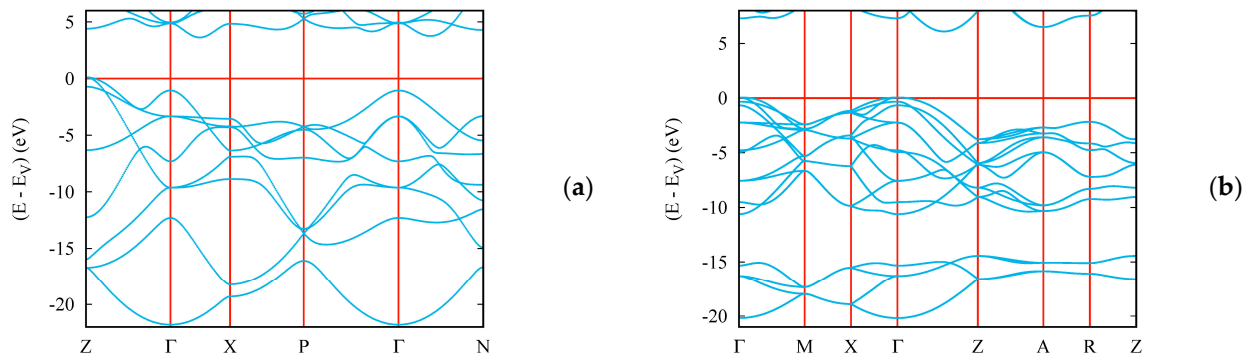


**Figure 6.** Cont.

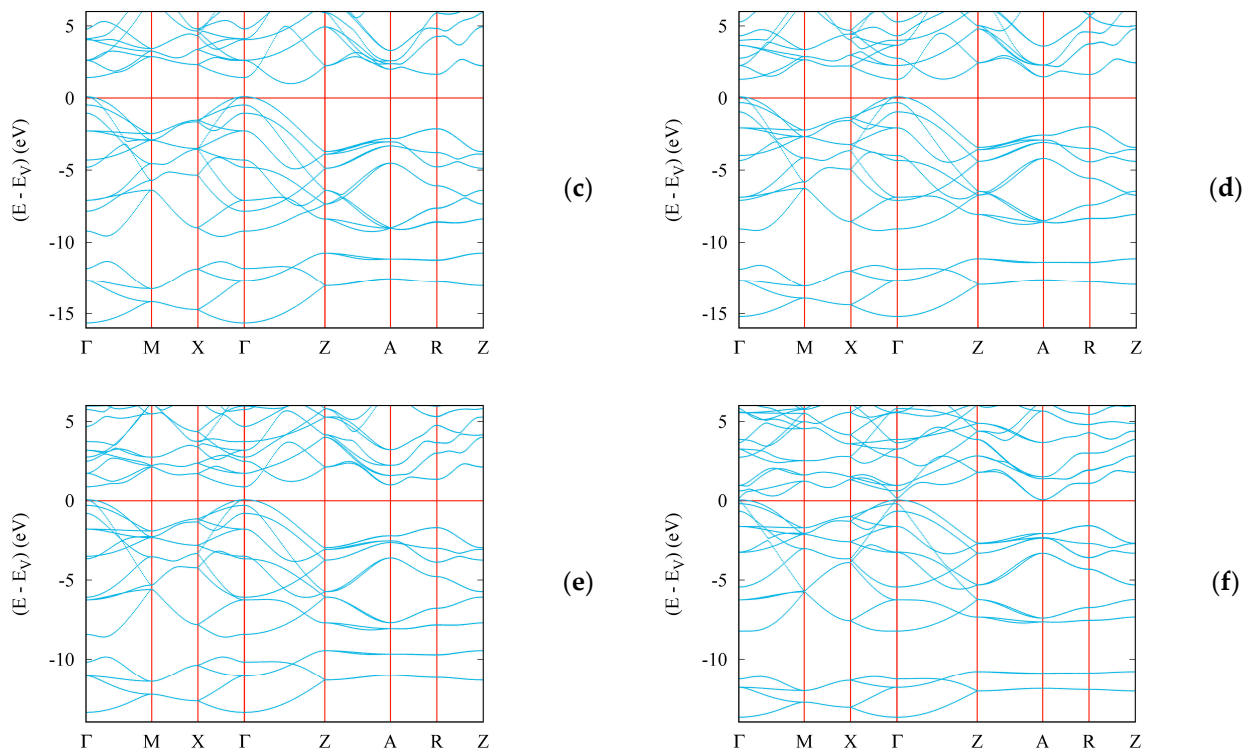


**Figure 6.** Electronic band structures (blue lines) of **crb** phases:  $C_8$  (a); BN (b); BP (c); BAs (d); BSb (e); BBi (f).

## 5. Conclusions

Based on crystal chemistry and density functional theory calculations, a novel family of tetragonal ( $P4_2/mnm$ ) boron pnictides BX with **crb** topology with X element belonging to group 5A ( $X = N, P, As, Sb, Bi$ ) was predicted. From a crystallographic point of view, these phases exhibit a square  $B2X2$  motif at  $z = 0$ , forming edge-sharing  $BX_4$  tetrahedra along the square diagonal, connected via corners along the vertical  $z$  direction. All new **crb** BX phases were found to be cohesive, and mechanically stable from elastic constants. As can be seen from the charge density projections, the BX family exhibits different types of chemical bonding, changing from nitride BN to ionocovalent behavior for P and As, and finally to borides in the case of Sb and Bi. A tendency for a significant decrease in hardness with increasing atomic number of the pnictogen was observed (from  $\sim 50$  GPa for BN to  $\sim 13$  GPa for BBi); however, all **crb** boron pnictides are hard phases with Vickers hardness exceeding (or equal to) that of cemented tungsten carbide, the conventional hard material. Dynamically, the new boron pnictides were found to be stable with positive phonon frequencies, except for  $X = Bi$ , which exhibits slightly negative acoustic phonons in the center of the Brillouin zone. The heat capacities of the **crb** BX calculated from the phonon frequencies were found to be slightly higher than those of the corresponding zinc-blende polymorphs, as expected for phases with increased openness of the crystal structures. From the analysis of the electronic band structures, it was found that the properties of the **crb** boron pnictides change from insulating to semiconducting along the series.

**Author Contributions:** Conceptualization, S.F.M.; methodology, S.F.M. and V.L.S.; investigation, S.F.M. and V.L.S.; formal analysis, S.F.M. and V.L.S.; data curation, S.F.M. and V.L.S.; visualization, S.F.M. and V.L.S.; validation, S.F.M. and V.L.S.; resources, S.F.M.; writing—original draft preparation, S.F.M.; writing—review and editing, V.L.S. All authors have read and agreed to the published version of the manuscript.

**Funding:** This research received no external funding.

**Data Availability Statement:** The data presented in this study are available on reasonable request.

**Conflicts of Interest:** The authors declare no conflicts of interest.

## References

1. Oganov, A.R.; Glass, C.W. Crystal structure prediction using ab initio evolutionary techniques: Principles and applications. *J. Chem. Phys.* **2006**, *124*, 244704. [[CrossRef](#)]
2. Merchant, A.; Batzner, S.; Schoenholz, S.S.; Aykol, M.; Cheon, G.; Cubuk, E.D. Scaling deep learning for materials discovery. *Nature* **2023**, *624*, 80–85. [[CrossRef](#)]
3. Glass, C.W.; Oganov, A.R.; Hansen, N. USPEX—Evolutionary crystal structure prediction. *Comput. Phys. Comm.* **2006**, *175*, 713–720. [[CrossRef](#)]
4. Hohenberg, P.; Kohn, W. Inhomogeneous electron gas. *Phys. Rev. B* **1964**, *136*, 864–871. [[CrossRef](#)]
5. Kohn, W.; Sham, L.J. Self-consistent equations including exchange and correlation effects. *Phys. Rev. A* **1965**, *140*, 1133–1138. [[CrossRef](#)]
6. Shevchenko, A.P.; Shabalin, A.A.; Karpukhin, I.Y.; Blatov, V.A. Topological representations of crystal structures: Generation, analysis and implementation in the *TopCryst* system. *Sci. Technol. Adv. Mat.* **2022**, *2*, 250–265. [[CrossRef](#)]
7. Prasad, D.L.V.K.; Gerovac, N.M.; Bucknum, M.J.; Hoffmann, R. Squaroglitter: A 3,4-connected carbon net. *J. Chem. Theory Comput.* **2013**, *9*, 3855–3859. [[CrossRef](#)]
8. Bucknum, M.J.; Hoffmann, R. A hypothetical dense 3,4-connected carbon net and related B<sub>2</sub>C and CN<sub>2</sub> nets built from 1,4-cyclohexadienoid units. *J. Am. Chem. Soc.* **1994**, *116*, 11456–11464. [[CrossRef](#)]
9. Hoffmann, R.; Kabanov, A.A.; Golov, A.A.; Proserpio, D.M. Homo Citans and carbon allotropes: For an ethics of citation. *Angew. Chem. Int. Ed.* **2016**, *55*, 10962–10976. [[CrossRef](#)] [[PubMed](#)]
10. Matar, S.F.; Solozhenko, V.L. Ultrahigh-density superhard hexagonal BN and SiC with quartz topology from crystal chemistry and first principles. *Crystals* **2023**, *13*, 1498. [[CrossRef](#)]
11. Solozhenko, V.L.; Matar, S.F. Superdense hexagonal BP and AlP with quartz topology: Crystal chemistry and DFT study. *Crystals* **2023**, *13*, 1622. [[CrossRef](#)]
12. Solozhenko, V.L.; Matar, S.F. High-pressure phases of boron pnictides BX (X = As, Sb, Bi) with quartz topology from first principles. *Crystals* **2024**, *14*, 221. [[CrossRef](#)]
13. Kresse, G.; Furthmüller, J. Efficient iterative schemes for ab initio total-energy calculations using a plane-wave basis set. *Phys. Rev. B* **1996**, *54*, 11169. [[CrossRef](#)]
14. Kresse, G.; Joubert, J. From ultrasoft pseudopotentials to the projector augmented wave. *Phys. Rev. B* **1999**, *59*, 1758–1775. [[CrossRef](#)]
15. Blöchl, P.E. Projector augmented wave method. *Phys. Rev. B* **1994**, *50*, 17953–17979. [[CrossRef](#)]
16. Perdew, J.; Burke, K.; Ernzerhof, M. The Generalized Gradient Approximation made simple. *Phys. Rev. Lett.* **1996**, *77*, 3865–3868. [[CrossRef](#)] [[PubMed](#)]
17. Press, W.H.; Flannery, B.P.; Teukolsky, S.A.; Vetterling, W.T. *Numerical Recipes*, 2nd ed.; Cambridge University Press: New York, NY, USA, 1986.
18. Blöchl, P.; Jepsen, O.; Anderson, O. Improved tetrahedron method for Brillouin-zone integrations. *Phys. Rev. B* **1994**, *49*, 16223–16233. [[CrossRef](#)]
19. Methfessel, M.; Paxton, A.T. High-precision sampling for Brillouin-zone integration in metals. *Phys. Rev. B* **1989**, *40*, 3616–3621. [[CrossRef](#)]
20. Monkhorst, H.J.; Pack, J.D. Special k-points for Brillouin Zone integration. *Phys. Rev. B* **1976**, *13*, 5188–5192. [[CrossRef](#)]
21. Eyert, V. Basic notions and applications of the augmented spherical wave method. *Int. J. Quantum Chem.* **2000**, *77*, 1007–1031. [[CrossRef](#)]
22. Gaillac, R.; Pullumbi, P.; Coudert, F.X. ELATE: An open-source online application for analysis and visualization of elastic tensors. *J. Phys. Condens. Matter* **2016**, *28*, 275201. [[CrossRef](#)] [[PubMed](#)]
23. Voigt, W. Über die Beziehung zwischen den beiden Elasticitätsconstanten isotroper Körper. *Annal. Phys.* **1889**, *274*, 573–587. [[CrossRef](#)]
24. Mazhnik, E.; Oganov, A.R. A model of hardness and fracture toughness of solids. *J. Appl. Phys.* **2019**, *126*, 125109. [[CrossRef](#)]
25. Chen, X.Q.; Niu, H.; Li, D.; Li, Y. Modeling hardness of polycrystalline materials and bulk metallic glasses. *Intermetallics* **2011**, *19*, 1275–1281. [[CrossRef](#)]
26. Mukhanov, V.A.; Kurakevych, O.O.; Solozhenko, V.L. The interrelation between hardness and compressibility of substances and their structure and thermodynamic properties. *J. Superhard Mater.* **2008**, *30*, 368–378. [[CrossRef](#)]
27. Mukhanov, V.A.; Kurakevych, O.O.; Solozhenko, V.L. Hardness of materials at high temperature and high pressure. *Phil. Mag.* **2009**, *89*, 2117–2127. [[CrossRef](#)]
28. Lyakhov, A.O.; Oganov, A.R. Evolutionary search for superhard materials: Methodology and applications to forms of carbon and TiO<sub>2</sub>. *Phys. Rev. B* **2011**, *84*, 092103. [[CrossRef](#)]
29. Mukhanov, V.A.; Kurakevych, O.O.; Solozhenko, V.L. Thermodynamic model of hardness: Particular case of boron-rich solids. *J. Superhard Mater.* **2010**, *32*, 167–176. [[CrossRef](#)]
30. Solozhenko, V.L.; Matar, S.F. Prediction of novel ultrahard phases in the B–C–N system from first principles: Progress and problems. *Materials* **2023**, *16*, 886. [[CrossRef](#)]

31. Solozhenko, V.L.; Bushlya, V. Mechanical properties of boron phosphides. *J. Superhard Mater.* **2019**, *41*, 84–89. [[CrossRef](#)]
32. Solozhenko, V.L. Hardness of new boron-rich chalcogenides B<sub>12</sub>S and B<sub>12</sub>Se. *J. Superhard Mater.* **2021**, *43*, 375–377. [[CrossRef](#)]
33. Solozhenko, V.L. On hardness of boron subarsenide B<sub>12</sub>As<sub>2</sub>. *J. Superhard Mater.* **2022**, *44*, 377–378. [[CrossRef](#)]
34. Brookes, C.A. The mechanical properties of cubic boron nitride. In *Science of Hard Materials. Proceedings of the International Conference*; Adam Hilger Ltd.: Accord, MA, USA, 1986; pp. 207–220.
35. Birch, F. Finite strain isotherm and velocities for single-crystal and polycrystalline NaCl at high pressures and 300 K. *J. Geophys. Res.* **1978**, *83*, 1257–1268. [[CrossRef](#)]
36. Togo, A.; Tanaka, I. First principles phonon calculations in materials science. *Scr. Mater.* **2015**, *108*, 1–5. [[CrossRef](#)]
37. Krishnan, R.S. Raman spectrum of diamond. *Nature* **1945**, *155*, 171. [[CrossRef](#)]
38. Dove, M.T. *Introduction to Lattice Dynamics*; Cambridge University Press: New York, NY, USA, 1993.
39. DeSorbo, W. Specific heat of diamond at low temperatures. *J. Chem. Phys.* **1953**, *21*, 876–880. [[CrossRef](#)]
40. Victor, A.C. Heat capacity of diamond at high temperatures. *J. Chem. Phys.* **1962**, *36*, 1903–1911. [[CrossRef](#)]
41. Solozhenko, V.L.; Gavrichev, K.S. Thermodynamic properties of boron nitride. In *Wide Band Gap Electronic Materials*; Preles, M.A., Gielisse, P., Popovici, G., Spitsyn, B.V., Stacy, T., Eds.; Kluwer Academic Publishers: Dordrecht, The Netherlands, 1995; pp. 377–392.
42. Ohsawa, J.; Nishinaga, T.; Uchiyama, S. Measurement of specific heat of boron monophosphide by AC calorimetry. *Jpn. J. Appl. Phys.* **1978**, *17*, 1059–1065. [[CrossRef](#)]
43. Koshchenko, V.I.; Grinberg, Y.K.; Demidenko, A.F. Thermodynamic properties of AlN (5–2700 K), GaP (5–1500 K) and BP (5–800 K). *Izv. Akad. Nauk SSSR Neorg. Mater.* **1984**, *20*, 1787–1790. (In Russian)
44. Kang, J.S.; Li, M.; Wu, H.; Nguyen, H.; Hua, Y. Basic physical properties of cubic boron arsenide. *Appl. Phys. Lett.* **2019**, *115*, 122103. [[CrossRef](#)]
45. Koshchenko, V.I.; Demidenko, A.F.; Grinberg, Y.K.; Yachmenev, V.E. Specific-heat and thermodynamic functions of BP, BAs and B<sub>6</sub>As at 5–310 K. *Izv. Akad. Nauk SSSR Neorg. Mater.* **1981**, *17*, 1965–1968. (In Russian)

**Disclaimer/Publisher’s Note:** The statements, opinions and data contained in all publications are solely those of the individual author(s) and contributor(s) and not of MDPI and/or the editor(s). MDPI and/or the editor(s) disclaim responsibility for any injury to people or property resulting from any ideas, methods, instructions or products referred to in the content.